Quantifying Non-Radiative Recombination in Passivated Wide-Bandgap Metal Halide Perovskites Using Absolute Photoluminescence Spectroscopy

Willemijn H. M. Remmerswaal, Bas T. van Gorkom, Dong Zhang, Martijn M. Wienk, and René A. J. Janssen*

Wide-bandgap (>1.6 eV) mixed-halide perovskites tend to experience notable open-circuit voltage losses in solar cells due to non-radiative recombination. Here, the effects of defects and their passivation on the non-radiative recombination of charge carriers in mixed-halide perovskite solar cells are studied. By determining the quasi-Fermi level splitting via absolute photoluminescence measurements of perovskite layers with and without charge transport layers, bulk and interface contributions are disentangled and compared to the radiative open-circuit voltage. For wide-bandgap perovskites, non-radiative recombination present in the pristine perovskite layers increases with increasing bandgap. The most prominent loss, located at the perovskite electron transport layer interface (ETL), can be reduced by interface passivation for the different bandgaps studied (1.58 to 1.82 eV) to a level close to that of the intrinsic losses. By combining light-intensity-dependent absolute photoluminescence spectroscopy with sensitive spectral photocurrent measurements it is found that different passivation agents result in a similar decrease of the non-radiative recombination for different bandgaps. This suggests that the gained open-circuit voltage is not due to an improved energy level alignment at the perovskite - ETL interface. Instead, passivation involves eliminating the direct contact between the perovskite semiconductor and the ETL.

W. H. M. Remmerswaal, B. T. van Gorkom, D. Zhang, M. M. Wienk, R. A. J. Janssen

Molecular Materials and Nanosystems and Institute for Complex Molecular Systems

Eindhoven University of Technology

P.O. Box 513, 5600 MB, Eindhoven The Netherlands

E-mail: r.a.j.janssen@tue.nl

D. Zhang

TNO

Partner in Solliance

High Tech Campus 21, 5656 AE, Eindhoven The Netherlands

R. A. J. Jansser

Dutch Institute for Fundamental Energy Research De Zaale 20, 5612 AJ, Eindhoven The Netherlands



The ORCID identification number(s) for the author(s) of this article can be found under https://doi.org/10.1002/aenm.202303664

© 2024 The Authors. Advanced Energy Materials published by Wiley-VCH GmbH. This is an open access article under the terms of the Creative Commons Attribution License, which permits use, distribution and reproduction in any medium, provided the original work is properly cited.

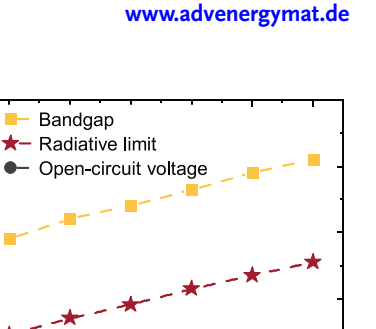
DOI: 10.1002/aenm.202303664

1. Introduction

In recent years, metal-halide perovskite solar cells (PSCs) have attracted enormous interest due to their large development rate, yielding an efficiency of 3.8%^[1] in 2009 to 26.1% in 2023 for just a single junction device.^[2] The combination of their excellent optoelectronic properties, solution-based fabrication, and easy bandgap tunability underlie the motivation of the extensive research in the photovoltaic community and significant progress.[3] For halide perovskites, with a nominal ABX3 crystal composition, the wide-bandgap absorber is typically obtained by mixing Br⁻ or Cl⁻ with I⁻ at the X-site, whereas a narrow bandgap is achieved by alloying Pb²⁺ with Sn²⁺ at the B-site.^[4,5] This allows for tuning the bandgap between 1.2 and 3 eV. Subsequently, PSCs hold the promise for low-cost, solution-processed, and high-efficiency all-perovskite tandem solar cells, resulting in all-perovskite and perovskitesilicon tandem solar cells at efficiencies

of 29.1% and 33.7%, respectively.[6]

Presently, wide-bandgap mixed-halide perovskites suffer from significant open-circuit voltage $(V_{\rm OC})$ losses. Clearly, a widebandgap top-cell yielding a high $V_{\rm OC}$ is critical to the efficiency of tandem devices. The main complication is that the $V_{\rm OC}$ of these wide-bandgap mixed-halide PSCs does not scale with the increase of the bandgap, because compositions containing higher bromide fractions tend to show a plateauing of the $V_{\rm OC}$ at ≈ 1.2 V. This $V_{\rm OC}$ deficit is caused by increased non-radiative charge recombination in these compositions due to defect states in the bulk, at grain interfaces, or charge-selective interfaces.^[7–11] Several mitigation strategies such as using additives like potassium iodide to improve the film quality and developing new charge transport materials, like self-assembled monolayers (SAMs) as a hole transporting material for p-i-n devices, to enable better energy alignment and minimized interfacial losses, have been investigated to address the voltage loss encountered in widebandgap perovskites.[12-14] After all these improvements, studies on the recombination processes show that the remaining,



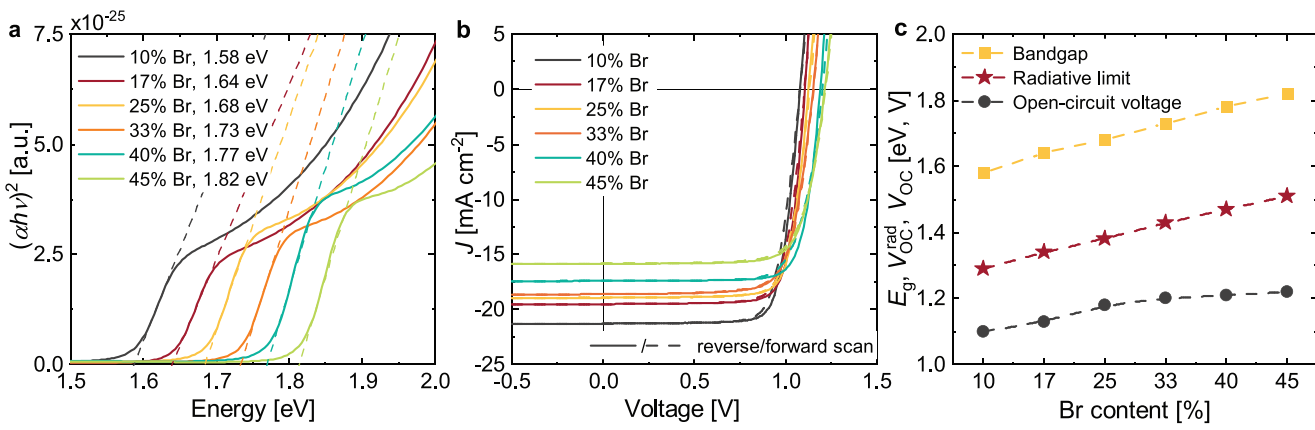


Figure 1. a) Tauc plots of perovskite films for different bromide concentrations to determine the bandgap energy (E_g) . b) J-V measurements in reverse (solid line) and forward (dashed line) scan directions (0.1 V s⁻¹ with voltage step of 0.02 V) under simulated AM 1.5G illumination calibrated to 100 mW cm⁻² of ITO | 2PACz | $C_{0.05}$ ($FA_{1-x}MA_x$)_{0.95} Pb($I_{1-x}Br_x$)₃ | C_{60} | BCP | Ag devices with different bromide concentrations (x). c) Bandgap (E_g), the radiative limit (V_{OC}^{rad}), and experimental V_{OC} versus the bromide concentration for the PSCs shown in panel b.

performance-limiting interface in a p-i-n device is the one between the perovskite and the electron transport layer (ETL), and that defects are primarily located at this interface. [9,15] The nonradiative recombination losses at the ETL interface are well described for some perovskite compositions in literature. [16–18] The loss could be due to trap states originating from an interaction between the perovskite and ETL or be a consequence of the possibility that there are simply more defects at the top surface of a perovskite.

Many passivation strategies have been employed to reduce non-radiative losses at the perovskite - ETL interface.[14] Previously, solution-processed quaternary ammonium halide salt (choline chloride, abbreviated as CCl)[19,20] or ultrathin evaporated lithium fluoride (LiF)[21-23] layers at this interface were found to induce a significant reduction of the voltage loss. As a passivation layer, the two materials yield the same result, even though the underlying mechanisms of these passivation strategies might differ. In fact, the exact origin of the passivating effects is not fully understood. A study on the effect of these passivation strategies for a consistent series of perovskites with different bandgaps is missing. To push efficiencies of wide-bandgap perovskite solar cells even further, voltage losses should be reduced and thus their mitigation strategies should be understood.

In this work, we examine the effect of passivation of defects at the perovskite - ETL interface on the non-radiative recombination of charge carriers in mixed-halide PSCs to understand the processes. We begin by analyzing the voltage loss for p-i-n devices and by investigating the passivation of defects of a midbandgap perovskite with a solution-processed CCl layer or a thermally evaporated LiF layer, which both translate to PSCs with a high $V_{\rm OC}$. We then extend this passivation study to a wider range of wide-bandgap perovskite devices. We find that non-radiative recombination in the pristine films increases with increasing bandgap. In a full device stack, non-radiative recombination at the perovskite - ETL interface dominates. Passivation of that interface reduces the non-radiative recombination almost to the level of the intrinsic perovskite. To further understand the working principle of the passivation strategies, we extend the passivation study by increasing the amount of passivation material and by performing light intensity-dependent absolute photoluminescence (PL) spectroscopy. Finally, by combining steady state and light intensity-dependent absolute PL spectroscopy with sensitive photocurrent measurements, we find that by using LiF or CCl in combination with C₆₀ as ETL, a significant reduction of the nonradiative recombination losses that currently limit wide-bandgap PSCs is achieved. The effect is ascribed to the spatial separation of the perovskite and C60 layers.

2. Results and Discussion

Mixed-halide perovskite $Cs_{0.05}(FA_{1-x}MA_x)_{0.95}Pb(I_{1-x}Br_x)_3$ thin films, with x = 0.10, 0.17, 0.25, 0.33, 0.40, and 0.45, were prepared and deposited on glass substrates according to earlier described methods (see the Supporting Information).^[24] As shown in Figure 1a, all mixed-halide perovskite films exhibited sharp absorption edges which shift to higher energies for increasing bromide concentration. The bandgaps (E_g) determined from the absorption onsets in the Tauc plots range from 1.58 eV for the lowest to 1.82 eV for the highest bromide concentration. These results are consistent with the bandgaps obtained from the maximum of the derivative of the external quantum efficiency (EQE) spectra of corresponding PSCs (10% bromide ≈1.59 eV and 45% ≈1.83 eV) (Figure S1, Supporting Information). [25] As expected, the bandgap increases proportionally with increasing bromide concentration.

To study the electronic properties and performance as a function of the increasing bandgap of these mixed-halide perovskites, PSCs were fabricated. The perovskite layer was deposited on a glass substrate with a patterned indium tin oxide (ITO) front electrode covered by a [2-(9H-carbazol-9-yl) ethyl] phosphonic acid (2PACz) SAM as hole transport layer (HTL). Fullerene (C₆₀) and bathocuproine (BCP) were used as ETL between the perovskite and the Ag back electrode. Figure 1b shows the current-density versus voltage (J-V) characteristics in forward and reverse scans of these mixed-halide ITO | 2PACz | perovskite | C₆₀ | BCP | Ag PSCs under simulated AM 1.5G illumination calibrated to 100 mW cm^{-2} . The hysteresis-free J-V scans show that the best device with the lowest bandgap (10% bromide) yields a $V_{\rm OC}$ of

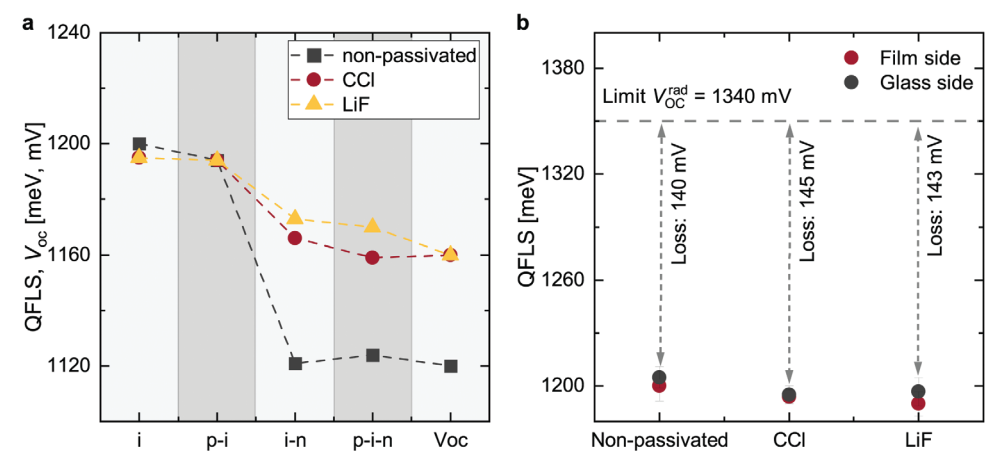


Figure 2. a) The QFLS of $Cs_{0.05}$ ($FA_{0.83}$ MA_{0.17})_{0.95} Pb($I_{0.83}$ Br_{0.17})₃ films without CTLs (i), with HTL (p-i), with ETL (i-n), and with HTL and ETL (p-i-n) and the V_{OC} of the corresponding solar cell, for films without and with passivation (CCl or LiF). b) QFLS of $Cs_{0.05}$ ($FA_{0.83}$ MA_{0.17})_{0.95} Pb($I_{0.83}$ Br_{0.17})₃ layers with and without passivation on top compared to the corresponding $V_{OC}^{rad} = 1.34$ V, measured with illumination from the film (top) or glass substrate (bottom) side. The QFLS obtained for the neat layer (i) is impacted by non-radiative recombination losses in the bulk. The QFLS of the partial stacks on glass substrates (p-i, i-n, and p-i-n) is impacted by additional interfacial recombination. The negligible difference between the QFLS of the p-i-n stack and the V_{OC} of the complete cell indicates that minimal losses occur at the metal electrodes due to non-radiative recombination or energy level alignment offsets.

1.10 V, a short-circuit current density ($J_{\rm SC}$) of 21.9 mA cm⁻², and a fill factor (FF) of 0.81, leading to a power conversion efficiency (PCE) of 18.6%. The best device with the highest bandgap (45% bromide) yields a $V_{\rm OC}$ of 1.21 V, a $J_{\rm SC}$ of 15.9 mA cm⁻², and a FF of 0.77, leading to a PCE of 14.6%. The EQE of all devices approaches 90% under 1-sun equivalent bias illumination (Figure S2, Supporting Information). Moreover, $J_{\rm SC}$ calculated from the integrated product of the EQE and the spectral irradiance of AM 1.5G spectrum at 1-sun solar intensity match. The device parameters are summarized in Table S1 and Figure S3 (Supporting Information) shows the boxplots containing all device parameters.

From detailed balance, it is expected that the $V_{\rm OC}$ will increase with increasing bandgap, while the $J_{\rm SC}$ will decrease concomitantly. [26,27] This is depicted in Figure 1c, where the measured bandgap and radiative open-circuit voltage limit ($V_{\rm OC}^{\rm rad}$) from detailed balance for all 6 different bromide concentrations are plotted versus the bromide concentration. Figure 1c also shows that the $V_{\rm OC}$ of these wide-bandgap mixed-halide PSCs does not scale proportionally with the bandgap, since compositions containing bromide concentrations above 25% show a plateauing $V_{\rm OC}$ at \approx 1.2 V. Thereby a bigger gap to the radiative limit is created for the wide-bandgap mixed-halide PSCs, indicating more non-radiative losses are suffered in these wide-bandgap mixed-halide PSCs.

Further improving these solar cells involves eliminating all possible losses, of which the loss between $V_{\rm OC}^{\rm rad}$ and $V_{\rm OC}$ is the most intriguing one. This voltage difference is a result of non-radiative recombination of electrons and holes. Non-radiative recombination, however, can be reduced as it occurs at defects, at grain boundaries, at interfaces, and trap sites. [14,28] However, in a PSC it is difficult to spatially resolve the non-radiative recombination. Measuring the $V_{\rm OC}$ of a PSC will not give the full answer, because the $V_{\rm OC}$ is measured at the device's external contacts. Given the multilayer architecture of PSCs, the $V_{\rm OC}$ cannot distinguish between losses in the absorber layer and its intrinsic defects, and

losses at the absorber – charge transport layer (CTL) interfaces and their defects. Instead, it yields an overall result.

To understand the origin of the non-radiative losses that reduce the V_{OC}, one can measure the quasi-Fermi level splitting (QFLS), i.e. the difference in the Fermi energy of holes and electrons under non-equilibrium conditions created by sunlight. The $qV_{\rm OC}$ and QFLS are interchangeable quantities and are often considered to be equal to each other. [26,29] One should note, however, that the QFLS is the difference between the electron and hole quasi-Fermi levels in the perovskite layer, whereas $qV_{\rm OC}$ stands for the difference between these levels at the cathode and the anode. When there is no bending of the quasi-Fermi levels and each of them aligns with the respective electrode work function, then QFLS = qV_{OC} . The absolute Fermi energies of holes and electrons are generally not accessible, but the QFLS can be determined directly by means of absolute PL measurements.[30-32] This methodology has proven to be an efficient approach for quantifying energy losses in the neat perovskite films, multilayer assemblies, and even complete perovskite solar cells.

Figure 2a depicts the quantified energy losses in specific layers through a comparison of the QFLS of different perovskite/transport layers of the 17% bromide triple cation perovskite $(Cs_{0.05}(FA_{0.83}MA_{0.17})_{0.95}Pb(I_{0.83}Br_{0.17})_3)$, for a configuration with no passivation and with two different passivation agents (CCl and LiF) on top. The corresponding absolute PL spectra of these measurements can be found in Figure S4 (Supporting Information). By first comparing the measured QFLS of the neat triple cation perovskite film (1.20 eV) to $V_{\rm OC}^{\rm rad} = 1.34 \text{ V}$ for $E_{\rm g}$ = 1.64 eV, significant non-radiative recombination losses are already observed (≈140 mV) in the bulk. When the perovskite is processed on top of a 2PACz HTL a negligible additional loss occurs. It is known that a 2PACz SAM has good band alignment to the valence band of the perovskite absorber, leading to low energetic loss at the perovskite - HTL interface.[19] Upon application of a thermally evaporated C_{60} ETL on top of the perovskite

www.advenergymat.de

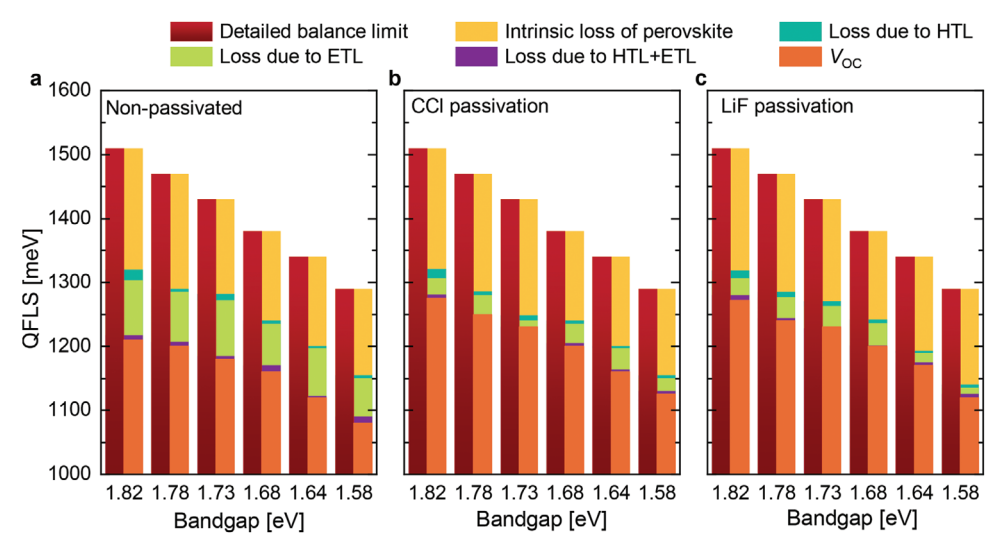


Figure 3. QFLS of the neat perovskite layers (i) and partial cell stacks on glass substrates (p-i, i-n, and p-i-n) and V_{OC} values of corresponding devices for six different bandgaps. a) Without top passivation. b) With CCl top passivation. c) With LiF top passivation. The radiative limits (red bars) are calculated from the corresponding bandgaps. Comparison with the intrinsic loss of the neat perovskite (yellow bars), the loss at the HTL – perovskite (blue-green bars), the loss of the perovskite – ETL interface (light green bars), the loss of the complete p-i-n configuration (purple bars), and the V_{OC} (orange bars) enables determining the different contributions to the non-radiative recombination.

To minimize non-radiative recombination losses and increase the $V_{\rm OC}$, first the main loss at the perovskite – ETL interface should be reduced, before addressing the non-radiative processes that remain in the perovskite itself. Different passivation strategies have been employed to reduce non-radiative losses at the perovskite – ETL interface. A solution-processed CCl or an ultrathin-evaporated LiF [21,22] layer at this interface was found to significantly reduce voltage losses on many occasions. In literature, it is stated that the first improves the $V_{\rm OC}$ by passivating both types of charged ionic defects, whereas the latter improves $V_{\rm OC}$ due to field effect passivation. Orrespondingly, Figure 2a shows that the loss in QFLS at the perovskite – ETL interface is minimized after the deposition of both CCl or LiF on top of the perovskite. Recently even better advancements have been achieved with piperazinium iodide.

Figure 2b shows the QFLS of the neat absorber layer with and without passivation on top passivation and their imminent losses with respect to the radiative limit for a 17% bromide perovskite. We can see the QFLS of the non-passivated films is 1200 ± 6 meV, i.e. ≈ 140 mV below the detailed balance limit (1340 mV based on a bandgap of 1.64 eV) and that the QFLS of the film with CCl and LiF passivated films are 1195 ± 5 and 1197 ± 9 meV, i.e. ≈ 145 and 143 mV below the detailed balance limit, respectively. Because the QFLS of the neat perovskite films is virtually independent of

the applied passivation, the reduction of the non-radiative losses in the complete p-i-n stack is not a result of LiF or CCl improving the bulk of the perovskite film or its top surface, but rather a result of an improvement on the perovskite – ETL interface. This also holds for the enhanced $V_{\rm OC}$.

To extend the study and understanding of the underlying principles of the passivation employed on top of the perovskite films, an analysis of each component in the PSC configuration to the non-radiative recombination for the six different bandgaps was carried out. For that purpose, six $Cs_{0.05}(FA_{1-x}MA_x)_{0.95}Pb(I_{1-x}Br_x)_3$ perovskites with $0.10 \le x \le$ 0.45 were prepared (see the Supporting Information) and the absolute PL was measured on all partial stacks of these PSCs. Figure 3 depicts the quantified QFLS losses for the six different bandgap triple cation perovskites in configurations without passivation and with CCl or LiF passivation. There was no indication of halide segregation while performing absolute PL measurements for all perovskite compositions, as can be seen in the examples of the absolute PL spectra and the normalized spectra (Figure S5 Supporting Information). The orange bar represents the $V_{\rm OC}$ of the devices under operation, and the other bars represent the limitation of each component present in the device stack for each bandgap. The losses are derived from subtracting the found QFLS value per interface (Figure S6, Supporting Information) from the radiative limit or the previous step in the layer configuration. We note that the QFLS of the individual stacks should be considered as a limit that can be reached. Without passivation, introduction of the ETL on top of the perovskite increases the non-radiative dark saturation currents $(J_{0.nr})$ by more than one order of magnitude (Figure S6, Supporting Information). This signifies that the perovskite - ETL interfacial recombination significantly exceeds the bulk losses.

Figure 3 shows that the $V_{\rm OC}$ of the wider bandgap compositions plateaus at ≈ 1.2 V without passivation at the perovskite – C_{60} interface, but is significantly increased once the CCl of LiF



www.advenergymat.de

interlayer is added. The intrinsic loss of the perovskite neat film increases with increasing bandgap. At $E_{\rm g}=1.58$ eV, where $V_{\rm OC}^{\rm rad}=1.29$ V, the perovskite suffers an intrinsic loss of 135 meV, but this increases to 190 meV for the perovskite with $E_{\rm g}=1.82$ eV where $V_{\rm OC}^{\rm rad}=1.51$ V. Hence, wider bandgap perovskite semiconductors are intrinsically more prone to higher $V_{\rm OC}$ losses. Surprisingly, top passivation by CCl or LiF has a minimal effect on the QFLS of the neat perovskite absorber layers. Importantly, this implies that the enhancement of the $V_{\rm OC}$ observed by applying CCl or LiF, cannot be the result of a passivation of the top surface of the perovskite film, but is a result of passivation of the perovskite – ETL interface.

Figure 3 also shows that the additional QFLS loss at the 2PACz – perovskite interface is minimal and does not change significantly as the bandgap increases (blue-green bars in Figure 3). Hence the 2PACz – perovskite interface is not limiting the performance for any of the studied perovskite compositions. Apparently, the energy levels remain sufficiently well-aligned for each bandgap studied even though the perovskite valence band changes with changing composition. This is in agreement with numerous studies that have shown that SAMs, like 2PACz, are excellent HTLs and that show the effect of energy alignment and interfacial recombination on the QFLS and $V_{\rm OC}$ of perovskite solar cells. $^{[12,15,35]}$

The most significant contribution to QFLS loss originates from the perovskite - C₆₀ interface. Compared to the pristine perovskite the additional loss between 65 and 87 meV remains fairly constant when increasing the bandgap, which indicates that in each case the loss at that interface dominates. The additional QFLS loss at the perovskite - C₆₀ interface is reduced to 15 to 35 meV after applying CCl or LiF on top of the perovskite (green bars in Figure 3). This implies that the intrinsic and interfacial losses are becoming more similar in magnitude. Since the morphologies are similar (Figure S7, Supporting Information), the fact that exchanging iodide for bromide leads to significant changes in both the valence band maximum and the conduction band minimum,[34] and the fact that the loss is similar for all bandgaps, we suggest that a common interfacial recombination process dominates this QFLS loss. It also implies that similar to the 2PACz – perovskite interface, the energy level alignment at the (passivated) perovskite - C₆₀ interface does not have a large effect on the QFLS loss. However, the effect of energy alignment remains partially unresolved, as the recombination currents at the ETL interface increase with an increasing bandgap. Nonetheless, large QFLS gradients due to a large energy level mismatch can be excluded. Finally, the additional QFLS loss when both 2PACz and C_{60} are used is minimal (purple bars in Figure 3). Although recent work has shown that there can be a mismatch between the QFLS and the $V_{\rm QC}$, [36] the QFLS determined from the complete p-i-n stack (purple bars in Figure 3) is in each case very close to actual the $V_{\rm OC}$ of the cell (orange bars in Figure 3) and confirms the validity of the analysis. Application of CCl and LiF thus improves the $V_{\rm OC}$ by reducing non-radiative recombination at the perovskite $-C_{60}$ interface and does so with virtually no losses in other device parameters, as shown in Figures \$8,\$9 (Supporting Information).

To further investigate the effect of the interface passivation, the sub-bandgap states of these mixed-halide perovskite solar cells and their defects were examined with sensitive photocurrent measurements that extend well below the bandgap to determine the EQE. A typical EQE spectrum in a semilogarithmic plot as a function of photon energy for a 17% bromide triple cation perovskite solar cell $(Cs_{0.05}(FA_{0.83}MA_{0.17})_{0.95}Pb(I_{0.83}Br_{0.17})_3)$ is shown in **Figure 4a**. This EQE spectrum can be divided into three distinct regions: the above-bandgap region, the band-tail region, and a subbandgap contribution. The above-bandgap region corresponds to the EQE spectrum presented in Figure S1 (Supporting Information). As the photon energy lowers to a value below the bandgap, there is an exponential decrease, known as the Urbach tail, which is caused by the energetic disorder within the perovskite material.[37] This Urbach tail arises due to band tailing of the valance and conduction bands. When the photon energy decreases even further, the EQE response starts to deviate from the Urbach tail and the signals that are observed in this region are attributed to sub-bandgap defect states.

In the sub-bandgap region, two distinct defects are present that are typical for mixed-halide perovskite solar cells. [9,38] One has to consider that the shape of the EQE spectrum in this region is significantly influenced by optical interference effects, resulting in a discrepancy between the true energetic distribution of sub-bandgap states and the EQE response that is measured. By exploiting these interference effects, previous work has demonstrated that in p-i-n devices the signals at 0.8 and 1.25 eV originate from sub-bandgap defects that are situated in proximity to the perovskite – fullerene interface. [9,10] Because the optical properties are nearly identical (the 1 nm of LiF or an ultrathin layer of CCl are optically not relevant), no optical corrections were applied. [9] Interestingly, the intrinsic defect shape also manifests in the sub-bandgap EQE of PSCs lacking CTLs, as shown in Figure \$10 (Supporting Information), which suggests that the fullerene is not directly responsible for this defect measured with sensitive EQE.

To measure a photocurrent, two main requirements need to be fulfilled; absorption of a photon resulting in an electron and hole pair, and the extraction of this electron and hole at opposite contacts. The difference between measuring the absorption of photons and detecting defects with sensitive EQE measurements stems from whether or not the photogenerated carriers can be extracted and a current can be measured. The defects measured by sensitive photocurrent spectroscopy are found to predominantly originate from the perovskite – ETL interface.^[9] Hence, we consider that during these measurements the extraction of electrons that are generated further away from this interface is limited, such that defects that are further from the interface do not contribute to the photocurrent. Consequently, this also implies that the transport of holes through the entire perovskite film is possible, whereas electrons are trapped, unless close to the collecting contact. Apparently, a metal electrode like gold (Figure S10, Supporting Information) can extract these trapped electrons when placed directly on top of the perovskite, but also a C₆₀ ETL can facilitate this (Figure 4a). In this scenario, the perovskite inherently harbors a defect and is detected by photocurrent spectroscopy when the electron is excited to a state where it can be extracted by a nearby electrode or ETL.

The effect of the interface passivation treatments for different bandgaps is investigated by examining the EQE response for all perovskite compositions without and with interface passivation

www.advenergymat.de

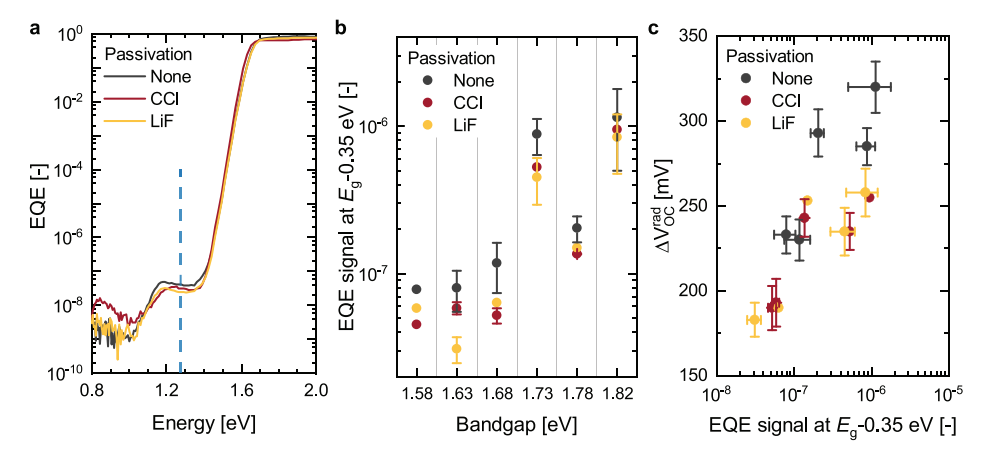


Figure 4. a) Semilogarithmic plot of the sensitive EQE spectra of 17% bromide triple cation perovskite solar cell with no passivation and with the two different passivation strategies. The response spaced 0.35 eV from the bandgap (E_g) is indicated with the blue dotted line. b) Semilogarithmic plot of the sensitive EQE response spaced 0.35 eV from the bandgap (E_g) for all the different bandgaps with no passivation and with two different passivation strategies. c) The ΔV_{CC}^{rad} as a function of the EQE response spaced 0.35 eV from the bandgap (E_g) for all PSCs with and without passivation. Error bars are included for data points where multiple experiments were performed.

treatment. The resulting EQE spectra (Figure S11, Supporting Information) have in general the same shape, with distinct signals in the sub-bandgap region, indicating that similar defects are present for all studied perovskite compositions. However, the defect signals at photon energies directly below the Urbach tail are higher for most wide-bandgap PSCs, supporting the idea that these devices suffer from increased bulk non-radiative losses.

To quantify this better, the EQE response recorded at 0.35 eV below the bandgap (E_{o} – 0.35 eV) is plotted in Figure 4b for the different perovskite compositions without and with CCl or LiF interface passivation. Figure 4b shows that CCl and LiF interface passivation both reduce the defect EQE at E_{o} - 0.35 eV for all bandgaps studied. Hence, the passivation layer effectively reduces the effect of defects for all bandgaps studied. However, the magnitude of this reduction of EQE is not constant throughout the studied range and the differences between the two interface passivation strategies occur intermittently. Moreover, the EQE response recorded 0.35 eV below the bandgap is subject to some experimental uncertainty for nominally identical devices (Figure S12, Supporting Information). Still, the reduction of the EQE signal indicates that both interface treatments reduce the defect contribution and help to mitigate the effect of these defects to a certain extent.

In Figure 4c, the $\Delta V_{\rm OC}^{\rm rad}$ (= $V_{\rm OC}^{\rm rad}$ – $V_{\rm OC}$) is shown versus the EQE at $E_{\rm g}$ – 0.35 eV in a semilogarithmic plot for the different PSCs without and with passivation. The plot shows that the voltage loss ($\Delta V_{\rm OC}^{\rm rad}$) increases with increasing defect signal intensity in the sub-bandgap EQE. Hence, the defect response in sensitive photocurrent measurements correlates (qualitatively) with the $V_{\rm OC}$ losses in a PSC. The scatter in the data indicates that the defects detected via sub-bandgap EQE are not the only contributing factor to $\Delta V_{\rm OC}^{\rm rad}$ and additional parameters need consideration for a quantitative correlation between EQE signal height and trap densities and an amount of trap densities. In Figure S12 (Supporting Information) more detail on the spread and error of the sensitive EQE data is provided.

To understand the interface passivation in more detail, the concentration of CCl and the thickness of LiF passivation were systematically increased for a 17% Br perovskite solar cell. The QFLS was examined using absolute PL measurements, while the subbandgap states and associated defects of these mixed-halide perovskite solar cells were investigated using sensitive photocurrent measurements. Figure 5a shows that the QFLS of the perovskite layer is independent of increasing the CCl layer thickness by using a more concentrated solution for the deposition (grey bars in Figure 5a). In contrast, the QFLS of the perovskite - C₆₀ combination reveals an increasing QFLS when using an increased concentration (and thickness) of the CCl interlayer (purple bars in Figure 5a). Likewise, the $V_{\rm OC}$ increases upon higher CCl concentration to a certain extend (open stars in Figure 5a). For the highest concentration, we see that the $V_{\rm OC}$, among the other performance parameters as shown in Figure S13 (Supporting Information), lowers again. Evidently, the enhancement in V_{OC} is directly proportional to the reduction of non-radiative recombination until it reaches a critical threshold, at which point the excessive thickness of the interlayer impedes the charge collection at the electrode. We observe identical behavior for the QFLS as a function of the LiF thickness (Figure 5c; Figure S14, Supporting Information).

Figure 5b,d shows the sensitive EQE spectra in a semilogarithmic plot as function of photon energy for a 17% bromide triple cation perovskite solar cell passivated with CCl for different concentrations and increasing LiF thicknesses. Upon the application of thicker interface passivation layers, a reduction of the defect signals at 1.25 eV is observed. For the CCl, the reduction in defect signal occurs rather non-uniformly, but continues to exhibit a declining trend for higher concentrations. When thicker layers of LiF are evaporated on top of the perovskite, the defect signal at 1.25 eV gradually decreases. This implies that both passivation layers effectively mitigate the effect of the fullerene layer in collecting electrons from photo-excited defects, and increasingly do so as for thicker layers.

-and-conditions) on Wiley Online Library for rules of use; OA articles are governed by the applicable Creative Commons License

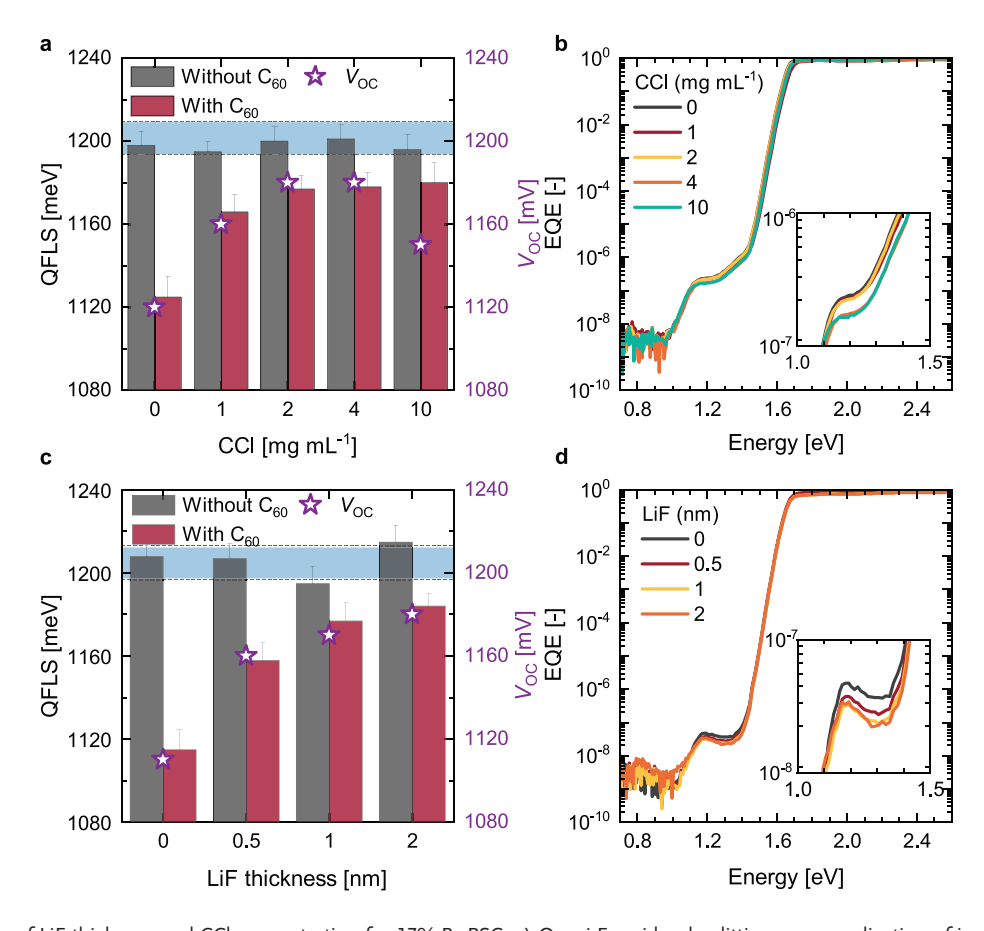


Figure 5. Influence of LiF thickness and CCl concentration for 17% Br PSC. a) Quasi-Fermi level splitting upon application of increasing the CCl concentration between the perovskite/ETL interface. The blue bar represents the average QFLS value of the perovskite film on glass without any passivation or CTL, the black bars represent the QFLS of the perovskite film, with a specified amount of passivation if applicable, the red bars represent the QFLS of the perovskite/ETL combination, with a specified amount of passivation if applicable. b) Semilogarithmic plot of the sensitive EQE spectra of the subbandgap region upon application of increasing the CCl concentration between the perovskite/ETL interface. The insert shows a further zoomed-in of the EQE response at the fullerene signal. c) Quasi-Fermi level splitting upon application of increasing LiF thickness between the perovskite/ETL interface and d) semilogarithmic plot of the sensitive EQE spectra of the sub-bandgap region upon application of increasing LiF thickness.

The reason for the reduced defect-EQE and improved passivation by thicker interlayers could simply be due to the increased spatial separation between perovskite and C₆₀ that diminishes the extraction of electrons excited from these defects. On the other hand, formation of very thin LiF layers by thermal evaporation has been reported to lead to the coalescence of similarly sized LiF nanoparticle islands on the surface, rather than a fully closed layer.[39,40] Crystallites, which are of comparable size, cover progressively smaller free areas until a full layer is formed at ≈3 nm. As deposition thickness reaches ≈0.5 nm, the coverage approaches 50%. [41] We note that the precise thickness at which a full layer forms depends on the specific deposition conditions, but that full layers will not be formed for LiF layers with thicknesses under 2 nm. The same can be expected for the solution-processed CCl layers, when low concentrations are used.[19,20,42] In this scenario, applying more LiF or CCl leads to a reduction in the contact area between the perovskite and the C₆₀ layer. This also impedes or reduces the likelihood of the transfer state occurring between the perovskite defect and the C₆₀ layer. Consequently,

the $V_{\rm OC}$ increases due to the reduction in non-radiative recombination.

By measuring the QFLS as a function of the light intensity, the pseudo (or implied) efficiency of a neat perovskite can be quantified.[43,44] Figure 6a shows the absolute PL spectra of a neat perovskite film recorded at different illumination intensities ranging from 0.002 to 2 sun equivalents. The resulting average QFLS as a function of the natural logarithm of the number of incident photons is shown in Figure 6b, in which each panel represents a certain layer combination. The first panel shows the data of a neat triple cation perovskite film (i) on glass, followed by the data of ITO | 2PACz | perovskite (p-i), glass | perovskite | C₆₀ (i-n), and ITO |2PACz | perovskite | C₆₀ (p-i-n) layer combinations. From the slope of the QFLS versus the natural logarithm of the number of incident photons, the radiative ideality factor $(n_{\rm ID})$ can be determined. The $n_{\rm ID}$ is related to the complex balance between bimolecular (band-to-band) recombination, trapassisted (Shockley-Read-Hall (SRH)) recombination, interface recombination, and recombination at the metal contacts. [45,46] The parameter $n_{\rm ID}$ can be determined either through fitting averaged

-and-conditions) on Wiley Online Library for rules of use; OA articles are governed by the applicable Creative Commons License



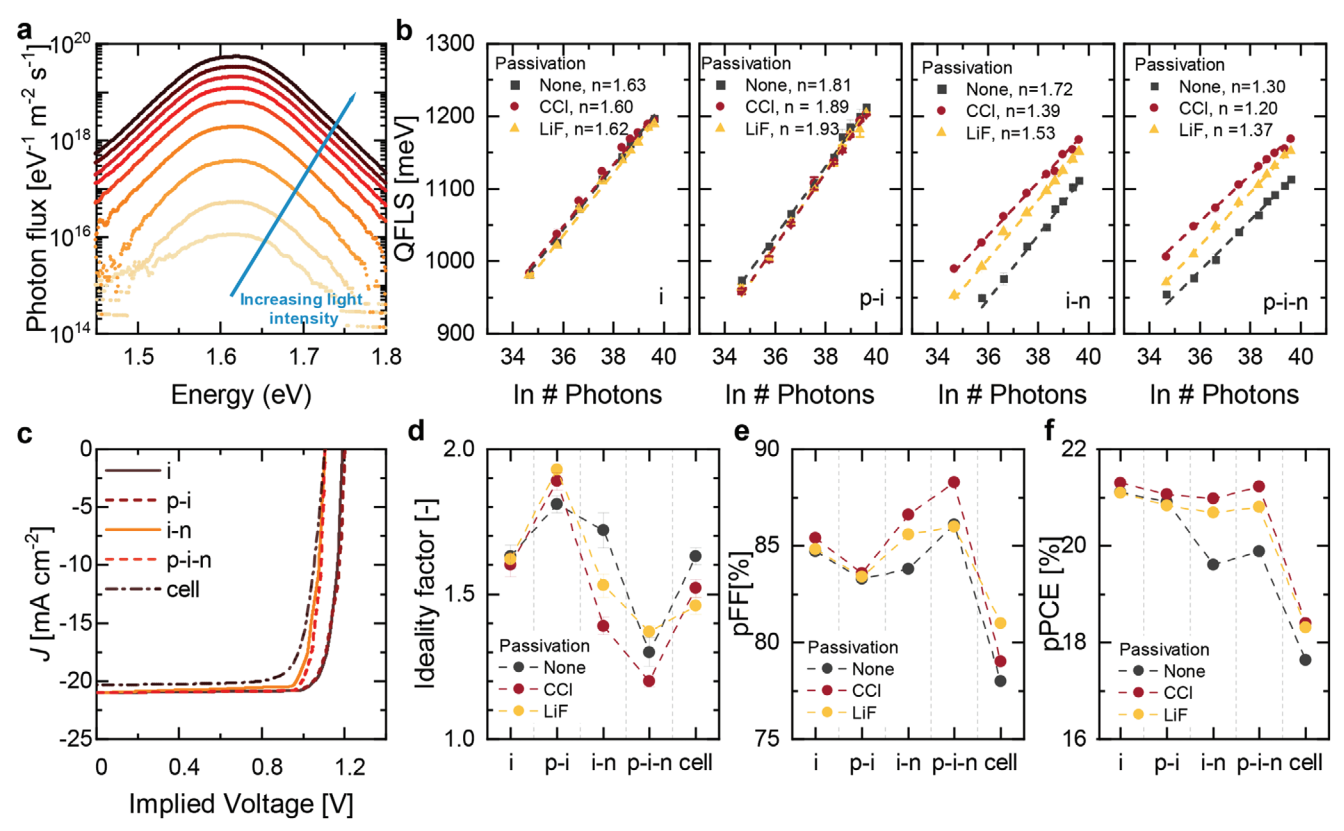


Figure 6. a) Example of intensity-dependent PL spectra as obtained on a neat triple cation perovskite film on glass from < 0.01 to 2 sun equivalents. b) The measured QFLS as a function of the natural logarithm of the number of incident photons for a neat triple cation perovskite film on glass, and ITO | 2PACz | perovskite, glass| perovskite | C_{60} and ITO | 2PACz | perovskite | C_{60} stacks. The ideality factor (n_{ID}) values extracted from fits of the data. c) Example of pseudo J-V curves of a neat triple cation perovskite film on glass, glass | perovskite | C_{60} , ITO | 2PACz | perovskite and ITO | 2PACz | perovskite | C_{60} stacks, and the real J-V curve of a completed device for comparison. d) Ideality factors (n_{ID}), e) pFF and FF, and f) pPCE and PCE from light intensity dependent measurements for the perovskite films on glass, the different interfaces and complete device combinations.

QFLS values as a function of light intensity or by fitting individual QFLS values as a function of light and subsequently averaging the obtained values. Figure S15 and Table S2 (Supporting Information) illustrate that there is minimal disparity. In our subsequent analysis, we opted for fitting averaged QFLS values as a function of light intensity.

We find that the neat perovskite films (i) on glass with and without passivation have nearly the same QFLS and the same light intensity dependence, with $n_{\rm ID} = 1.62 \pm 0.02$, a value that corresponds to earlier observations for neat perovskite films.^[45] Hence, applying CCl or LiF layers to the perovskite surface does not change the predominant recombination pathway for the neat film. The same occurs for the ITO | 2PACz | perovskite (p-i) configuration where $n_{\rm ID} = 1.88 \pm 0.06$ is also almost independent of surface passivation, but slightly higher than on glass. We note that perovskite grown on glass and ITO | 2PACz can be different and cause this change. Previously, based on drift-diffusion simulations, an $n_{\rm ID} \approx 1.8$ was found considering only bulk recombination (i.e., assuming ideal interfaces). [45] The third and fourth panels illustrate the effect of introducing the C_{60} layer for the glass | perovskite | C₆₀ (i-n) and ITO | 2PACz | perovskite | C₆₀ layer (p-i-n) configurations. As shown in Figures 2, 3, and 5, the QFLS is significantly reduced with a C₆₀ ETL on top of the perovskite and partially restored by interface passivation. In the p-i-n

configuration, the average $n_{\rm ID}\approx 1.29\pm 0.08$ corresponds to the ideality factor of ≈ 1.3 found by Caprioglio et al. [45] which, based on numerical simulations, was attributed to interfacial recombination at the C_{60} interface as the only cause. This is consistent with reduction of the QFLS when C_{60} is applied and partial recovery of interface passivation. For the passivated i-n configuration half-stacks, we find $n_{\rm ID}=1.46\pm 0.10$, which is slightly >1.3, but still indicates that recombination at the perovskite – C_{60} interface dominates. In our experiments, a higher QFLS corresponds with a larger $n_{\rm ID}$, consistent with previous observations. [45] The only exception, and unanswered question, is the non-passivated i-n configuration where $n_{\rm ID}=1.72$ and the QFLS is low. One could speculate that the interpretation of the $n_{\rm ID}$ value may become more complex due to changes in the build-in field when comparing diverse stacks.

Figure 6d summarizes these results and includes the $n_{\rm ID}$ values for the $V_{\rm OC}$. When interpreting $n_{\rm ID}$ it is paramount to concurrently consider the QFLS. Figure 6b shows that the highest QFLS occurs in the p-i configuration where $n_{\rm ID}$ is the highest. The lower QFLS (or $V_{\rm OC}$) for all other configurations (i, i-n, and p-i-n) is consistently accompanied by a smaller $n_{\rm ID}$, with the exception noted above. The co-occurrence of reduced QFLS and reduced $n_{\rm ID}$ values in the i-n and p-i-n configurations (with respect to their related i and p-i configurations) are consistent with



www.advenergymat.de

significant non-radiative recombination at the perovskite – ETL interface as inferred from Figure 3.

As the QFLS under illumination represents the internal voltage multiplied by the elementary charge q, and considering that light intensity is proportional to the generated photocurrent, one can convert the QFLS-intensity curves to pseudo J-V curves. [38] From these pseudo J-V curves, one can derive the pseudo FF (pFF) and the pseudo PCE (pPCE), along with the pseudo-opencircuit voltage (QFLS at 1-sun equivalent) and the short-circuit current density. Pseudo J-V curves are shown in Figure 6c for each of the i, p-i, i-n, and p-i-n stacks together with the J-V curve of the complete device.

Figure 6e,f shows the pFF and pPCE. The differences in pFF are small for perovskite films on glass or on ITO | 2PACz, and independent of applying CCl or LiF on top. The neat perovskite films exhibit a pFF as high as 85%. Going from the neat perovskite film on glass to the film on ITO | 2PACz results in a slightly lower pFF, consistent with the increased ideality factors. [47] For the perovskite | C₆₀ configuration, the pFF increases more when applying CCl and LiF, while it remains lower without passivation. These results show a clear improvement upon application of both surface treatments from the perovskite - C₆₀ interface. For the complete p-i-n stack, the pFF with the CCl is high, due to the very low ideality factor. The complete devices, however, still lose quite a significant amount of FF, likely caused by transport losses in the devices. Interestingly, the thin passivating interlayers do not increase these transport losses and passivated devices have higher efficiencies.

The pPCE reaches >21% for the perovskite films on glass and on ITO | 2PACz. When applying the C_{60} ETL on top of the perovskite, the film without passivation loses quite a bit pPCE, but the passivated films maintain high pPCE. The same applies to the complete p-i-n stacks. The complete devices, however, have a lower PCE than the pPCE of the p-i-n stack, likely due to additional transport losses in the device.

3. Conclusion

In this work, we have shown with absolute PL measurements that intrinsic non-radiative recombination losses of the studied perovskites increase with increasing bandgap and ultimately lead to a significant drop in $V_{\rm OC}$ and PCE. Interface passivation treatments do not decrease the non-radiative recombination losses in the bulk of these perovskites. Non-radiative recombination losses at the interface between the perovskite and the 2PACz HTL are negligible. In contrast, the perovskite $-C_{60}$ ETL interface is the dominant source of non-radiative recombination, independent of the bandgap. The non-radiative recombination loss at the perovskite – C₆₀ interface can be reduced by applying thin CCl or LiF interfacial passivation layers. CCl and LiF have a very similar effect, despite their chemical differences. Passivation results in an increase of the QFLS and pPCE for p-i-n stacks and of the $V_{\rm OC}$ and PCE of actual devices. Sensitive photocurrent measurements provide a possible explanation. We propose that the perovskite has inherent defects which can be photoexcited and produce a photocurrent when electrons can be extracted by a C₆₀ ETL (or a metal). The likelihood of the excitonic transfer state occurring between the perovskite defect and the fullerene transport layer

can be reduced by decreasing the contact area and/or increasing the spatial separation between the perovskite and the C_{60} layer.

Summarizing, the investigated passivation strategies, based on very different molecules (CCl or LiF) and deposition methods show the same effects in QFLS and sensitive EQE for all six investigated bandgaps. CCl and LiF do not passivate the surface (or bulk) of the perovskite but do passivate the interface with the C_{60} ETL. This points to a common mechanism for the passivation.

We note that these findings are not limited to the specific perovskite composition tested in this study and similar improvements in reducing non-radiative losses have been observed for other compositions. Nonetheless, it is important to consider that different perovskite compositions may exhibit different types and magnitudes of losses, and thus, further investigations are required to fully understand the passivation mechanisms and optimize the performance of perovskite solar cells.

Supporting Information

Supporting Information is available from the Wiley Online Library or from the author.

Acknowledgements

The authors thank Bruno Pinto Branco for SEM measurements and Guus Aalbers for additional EQE measurements. The authors are indebted to the reviewers for their guidance in improving the interpretation of the data. The authors acknowledge funding from the Netherlands Organization for Scientific Research (NWO Spinoza grant) and the Ministry of Education, Culture, and Science (Gravity program 024.001.035). The work was further part of the Advanced Research Center for Chemical Building Blocks, ARC CBBC, which was co-founded and co-financed by NWO and the Netherlands Ministry of Economic Affairs (project 2016.03.Tue).

Conflict of Interest

The authors declare no competing interests.

Data Availability Statement

The data that support the findings of this study are available from the corresponding author upon reasonable request.

Keywords

absolute photoluminescence, metal-halide perovskite, passivation, quasi-Fermi level splitting

> Received: October 29, 2023 Revised: January 25, 2024 Published online:

^[1] A. Kojima, K. Teshima, Y. Shirai, T. Miyasaka, J. Am. Chem. Soc. 2009, 131, 6050.

^[2] H. Min, D. Y. Lee, J. Kim, G. Kim, K. S. Lee, J. Kim, M. J. Paik, Y. K. Kim, K. S. Kim, M. G. Kim, T. J. Shin, S. Il Seok, *Nature* 2021, 598, 444.

ADVANCED ENERGY MATERIALS

www.advancedsciencenews.com

www.advenergymat.de

- [3] Y. Zhou, I. Poli, D. Meggiolaro, F. De Angelis, A. Petrozza, Nat. Rev. Mater. 2021, 6, 986.
- [4] J. Xu, C. C. Boyd, Z. J. Yu, A. F. Palmstrom, D. J. Witter, B. W. Larson, R. M. France, J. Werner, S. P. Harvey, E. J. Wolf, W. Weigand, S. Manzoor, M. F. A. M. van Hest, J. J. Berry, J. M. Luther, Z. C. Holman, M. D. McGehee, *Science* 2020, 367, 1097.
- [5] Z. Song, C. Chen, C. Li, R. A. Awni, D. Zhao, Y. Yan, Semicond. Sci. Technol. 2019, 34, 093001.
- [6] M. A. Green, E. D. Dunlop, M. Yoshita, N. Kopidakis, K. Bothe, G. Siefer, X. Hao, Prog. Photovolt. Res. Appl. 2023, 31, 651.
- [7] S. Mahesh, J. M. Ball, R. D. J. Oliver, D. P. McMeekin, P. K. Nayak, M. B. Johnston, H. J. Snaith, Energy Environ. Sci. 2020, 13, 258.
- [8] P. Chen, Y. Bai, L. Wang, Small Struct. 2021, 2, 2000050.
- [9] B. T. van Gorkom, T. P. A. van der Pol, K. Datta, M. M. Wienk, R. A. J. Janssen, *Nat. Commun.* 2022, 13, 349.
- [10] J. Warby, F. Zu, S. Zeiske, E. Gutierrez-Partida, L. Frohloff, S. Kahmann, K. Frohna, E. Mosconi, E. Radicchi, F. Lang, S. Shah, F. Peña-Camargo, H. Hempel, T. Unold, N. Koch, A. Armin, F. De Angelis, S. D. Stranks, D. Neher, M. Stolterfoht, Adv. Energy Mater. 2022, 12, 2103567.
- [11] M. Stolterfoht, C. M. Wolff, J. A. Márquez, S. Zhang, C. J. Hages, D. Rothhardt, S. Albrecht, P. L. Burn, P. Meredith, T. Unold, D. Neher, Nat. Energy 2018, 3, 847.
- [12] A. Al-Ashouri, A. Magomedov, M. Roß, M. Jošt, M. Talaikis, G. Chistiakova, T. Bertram, J. A. Márquez, E. Köhnen, E. Kasparavičius, S. Levcenco, L. Gil-Escrig, C. J. Hages, R. Schlatmann, B. Rech, T. Malinauskas, T. Unold, C. A. Kaufmann, L. Korte, G. Niaura, V. Getautis, S. Albrecht, *Energy Environ. Sci.* 2019, 12, 3356.
- [13] M. Abdi-Jalebi, Z. Andaji-Garmaroudi, S. Cacovich, C. Stavrakas, B. Philippe, J. M. Richter, M. Alsari, E. P. Booker, E. M. Hutter, A. J. Pearson, S. Lilliu, T. J. Savenije, H. Rensmo, G. Divitini, C. Ducati, R. H. Friend, S. D. Stranks, *Nature* 2018, 555, 497.
- [14] B. Chen, P. N. Rudd, S. Yang, Y. Yuan, J. Huang, Chem. Soc. Rev. 2019, 48, 3842.
- [15] M. Stolterfoht, P. Caprioglio, C. M. Wolff, J. A. Márquez, J. Nordmann, S. Zhang, D. Rothhardt, U. Hörmann, Y. Amir, A. Redinger, L. Kegelmann, F. Zu, S. Albrecht, N. Koch, T. Kirchartz, M. Saliba, T. Unold, D. Neher, *Energy Environ. Sci.* 2019, 12, 2778.
- [16] F. Peña-Camargo, P. Caprioglio, F. Zu, E. Gutierrez-Partida, C. M. Wolff, K. Brinkmann, S. Albrecht, T. Riedl, N. Koch, D. Neher, M. Stolterfoht, ACS Energy Lett. 2020, 45, 25.
- [17] S. Cacovich, G. Vidon, M. Degani, M. Legrand, L. Gouda, J.-B. Puel, Y. Vaynzof, J.-F. Guillemoles, D. Ory, G. Grancini, *Nat. Commun.* 2022, 13, 2868.
- [18] S. Zhang, P. E. Shaw, G. Zhang, H. Jin, M. Tai, H. Lin, P. Meredith, P. L. Burn, D. Neher, M. Stolterfoht, ACS Appl. Mater. Interfaces 2020, 12, 37656.
- [19] K. Datta, J. Wang, D. Zhang, V. Zardetto, W. H. M. Remmerswaal, C. H. L. Weijtens, M. M. Wienk, R. A. J. Janssen, Adv. Mater. 2022, 34, 2110053.
- [20] X. Zheng, B. Chen, J. Dai, Y. Fang, Y. Bai, Y. Lin, H. Wei, X. C. Zeng, J. Huang, Nat. Energy 2017, 2, 17102.
- [21] F. Penã-Camargo, P. Caprioglio, F. Zu, E. Gutierrez-Partida, C. M. Wolff, K. Brinkmann, S. Albrecht, T. Riedl, N. Koch, D. Neher, M. Stolterfoht, ACS Energy Lett. 2020, 5, 2728.
- [22] J. Liu, M. De Bastiani, E. Aydin, G. T. Harrison, Y. Gao, R. R. Pradhan, M. K. Eswaran, M. Mandal, W. Yan, A. Seitkhan, M. Babics, A. S. Subbiah, E. Ugur, F. Xu, L. Xu, M. Wang, A. ur Rehman, A. Razzaq, J. Kang, R. Azmi, A. Ali Said, F. H. Isikgor, T. G. Allen, D. Andrienko, U. Schwingenschlögl, F. Laquai, S. De Wolf, Science 2022, 377, 302.

- [23] D. Menzel, A. Al-Ashouri, A. Tejada, I. Levine, J. A. Guerra, B. Rech, S. Albrecht, L. Korte, Adv. Energy Mater. 2022, 12, 2201109.
- [24] M. Saliba, T. Matsui, J.-Y. Seo, K. Domanski, J.-P. Correa-Baena, M. Khaja, S. M. Zakeeruddin, W. Tress, A. Abate, A. Hagfeldt, M. Grätzel, Energy Environ. Sci. 2016, 9, 1989.
- [25] L. Krückemeier, U. Rau, M. Stolterfoht, T. Kirchartz, Adv. Energy Mater. 2020, 10, 1902573.
- [26] W. Shockley, H. J. Queisser, J. Appl. Phys. 1961, 32, 510.
- [27] S. Rühle, Sol. Energy 2016, 130, 139.
- [28] T. S. Sherkar, C. Momblona, L. Gil-Escrig, J. Ávila, M. Sessolo, H. J. Bolink, L. J. A. Koster, ACS Energy Lett. 2017, 2, 1214.
- [29] P. Würfel, J. Phys. C: Solid State Phys. 1982, 15, 3967.
- [30] D. Abou-Ras, T. Kirchartz, U. Rau, Advanced Characterization Techniques for Thin Film Solar Cells, 2nd ed., Wiley, Weinheim, Germany 2016.
- [31] T. Kirchartz, U. Rau, Physica Status Solidi 2008, 205, 2737.
- [32] P. Würfel, U. Würfel, Physics of Solar Cells: From Basic Principles to Advanced Concepts, 3rd ed., Wiley, Weinheim, Germany 2016.
- [33] S. Mariotti, E. Köhnen, F. Scheler, K. Sveinbjörnsson, L. Zimmermann, M. Piot, F. Yang, B. Li, J. Warby, A. Musiienko, D. Menzel, F. Lang, S. Keßler, I. Levine, D. Mantione, A. Al-Ashouri, M. S. Härtel, K. Xu, A. Cruz, J. Kurpiers, P. Wagner, H. Köbler, J. Li, A. Magomedov, D. Mecerreyes, E. Unger, A. Abate, M. Stolterfoht, B. Stannowski, R. Schlatmann, et al., Science 2023, 381, 63.
- [34] S. Tao, I. Schmidt, G. Brocks, J. Jiang, I. Tranca, K. Meerholz, S. Olthof, Nat. Commun. 2019, 10, 2560.
- [35] A. Magomedov, A. Al-Ashouri, E. Kasparavičius, S. Strazdaite, G. Niaura, M. Jošt, T. Malinauskas, S. Albrecht, V. Getautis, Adv. Energy Mater. 2018, 8, 1801892.
- [36] J. Warby, S. Shah, J. Thiesbrummel, E. Gutierrez-Partida, H. Lai, B. Alebachew, M. Grischek, F. Yang, F. Lang, S. Albrecht, F. Fu, D. Neher, M. Stolterfoht, Adv. Energy Mater. 2023, 2303135.
- [37] V. M. Caselli, Z. Wei, M. M. Ackermans, E. M. Hutter, B. Ehrler, T. J. Savenije, ACS Energy Lett. 2020, 5, 3821.
- [38] C. M. Sutter-Fella, D. W. Miller, Q. P. Ngo, E. T. Roe, F. M. Toma, I. D. Sharp, M. C. Lonergan, A. Javey, ACS Energy Lett. 2017, 2, 700
- [39] A. Turak, Electron. Mater. 2021, 2, 198.
- [40] L. G. Schulz, J. Chem. Phys. 1949, 17, 1153.
- [41] S. Il Lee, K. Liang, L. S. Hui, R. Arbi, M. Munir, S. J. Lee, J. W. Kim, K. J. Kim, W. Y. Kim, A. Turak, J. Mater. Sci.: Mater. Electron. 2021, 32, 1161.
- [42] X. Xu, K. Xiao, G. Hou, Y. Zhang, T. Zhu, L. Xu, J. Xu, K. Chen, Adv. Opt. Mater. 2021, 9, 2100636.
- [43] M. Stolterfoht, M. Grischek, P. Caprioglio, C. M. Wolff, E. Gutierrez-Partida, F. Peña-Camargo, D. Rothhardt, S. Zhang, M. Raoufi, J. Wolansky, M. Abdi-Jalebi, S. D. Stranks, S. Albrecht, T. Kirchartz, D. Neher, Adv. Mater. 2020, 32, 2000080.
- [44] M. Grischek, P. Caprioglio, J. Zhang, F. Peña-Camargo, K. Sveinbjörnsson, F. Zu, D. Menzel, J. H. Warby, J. Li, N. Koch, E. Unger, L. Korte, D. Neher, M. Stolterfoht, S. Albrecht, Sol. RRL 2022, 6, 2200690.
- [45] P. Caprioglio, C. M. Wolff, O. J. Sandberg, A. Armin, B. Rech, S. Albrecht, D. Neher, M. Stolterfoht, Adv. Energy Mater. 2020, 10, 2000502.
- [46] W. Tress, M. Yavari, K. Domanski, P. Yadav, B. Niesen, J. P. Correa Baena, A. Hagfeldt, M. Grätzel, Energy Environ. Sci. 2018, 11, 151.
- [47] D. Grabowski, Z. Liu, G. Schöpe, U. Rau, T. Kirchartz, Sol. RRL 2022, 6, 2200507.